




3-23-2010

# Measurement of $\gamma$ -emission Branching Ratios for $^{154,156,158}\text{Gd}$ Compound Nuclei: Tests of Surrogate Nuclear Reaction Approximations for $(n,\gamma)$ Cross Sections

N. D. Scielzo

Follow this and additional works at: <http://scholarship.richmond.edu/physics-faculty-publications> Part of the [Atomic, Molecular and Optical Physics Commons](#), [Biological and Chemical Physics Commons](#), and the [Nuclear Commons](#)

## Recommended Citation

Scielzo, N. D., J. E. Escher, J. M. Allmond, M. S. Basunia, C. W. Beausang, L. A. Bernstein, D. L. Bleuel, J. T. Burke, R. M. Clark, F. S. Dietrich, P. Fallon, J. Gibelin, B. L. Goldblum, S. R. Leshner, M. A. McMahan, E. B. Norman, L. Phair, E. Rodriguez-Vieitez, S. A. Sheets, I. J. Thompson, and M. Wiedeking. "Measurement of  $\gamma$ -emission Branching Ratios for  $^{154,156,158}\text{Gd}$  Compound Nuclei: Tests of Surrogate Nuclear Reaction Approximations for  $(n,\gamma)$  Cross Sections." *Physical Review C* 81, no. 3 (March 23, 2010): 034608: 1-34608: 12. doi:10.1103/PhysRevC.81.034608.

# Measurement of $\gamma$ -emission branching ratios for $^{154,156,158}\text{Gd}$ compound nuclei: Tests of surrogate nuclear reaction approximations for $(n, \gamma)$ cross sections

N. D. Scielzo,<sup>1</sup> J. E. Escher,<sup>1</sup> J. M. Allmond,<sup>2</sup> M. S. Basunia,<sup>3</sup> C. W. Beausang,<sup>2</sup> L. A. Bernstein,<sup>1</sup> D. L. Bleuel,<sup>1</sup> J. T. Burke,<sup>1</sup> R. M. Clark,<sup>3</sup> F. S. Dietrich,<sup>1</sup> P. Fallon,<sup>3</sup> J. Gibelin,<sup>3</sup> B. L. Goldblum,<sup>4</sup> S. R. Lesher,<sup>1</sup> M. A. McMahan,<sup>3</sup> E. B. Norman,<sup>1,3,4</sup> L. Phair,<sup>3</sup> E. Rodriguez-Vieitez,<sup>3,4</sup> S. A. Sheets,<sup>1</sup> I. J. Thompson,<sup>1</sup> and M. Wiedeking<sup>1,3</sup>

<sup>1</sup>Physical Sciences Directorate, Lawrence Livermore National Laboratory, Livermore, California 94551, USA

<sup>2</sup>Department of Physics, University of Richmond, Richmond, Virginia 23173, USA

<sup>3</sup>Nuclear Science Division, Lawrence Berkeley National Laboratory, Berkeley, California 94720, USA

<sup>4</sup>Department of Nuclear Engineering, University of California, Berkeley, California 94720, USA

(Received 28 December 2009; published 23 March 2010)

The surrogate nuclear reaction method can be used to determine neutron-induced reaction cross sections from measured decay properties of a compound nucleus created using a different reaction and calculated formation cross sections. The reliability of  $(n, \gamma)$  cross sections determined using the Weisskopf-Ewing and ratio approximations are explored for the  $^{155,157}\text{Gd}(n, \gamma)$  reactions. Enriched gadolinium targets were bombarded with 22-MeV protons and  $\gamma$  rays were detected in coincidence with scattered protons using the Silicon Telescope Array for Reaction Studies/Livermore-Berkeley Array for Collaborative Experiments (STARS/LiBerACE) silicon and germanium detector arrays. The  $\gamma$ -emission probabilities for the  $^{154,156,158}\text{Gd}$  compound nuclei were measured at excitation energies up to 12 MeV. It is found that the approximations yield results that deviate from directly measured  $^{155,157}\text{Gd}(n, \gamma)$  cross sections at low energies. To extract reliable cross sections, a more sophisticated analysis should be developed that takes into account angular-momentum differences between the neutron-induced and surrogate reactions.

DOI: [10.1103/PhysRevC.81.034608](https://doi.org/10.1103/PhysRevC.81.034608)

PACS number(s): 24.87.+y, 24.60.Dr, 26.20.Kn, 25.60.Tv

## I. INTRODUCTION

Radiative neutron-capture reactions on unstable nuclei play an important role in many areas of basic and applied sciences. The synthesis of heavy elements by the astrophysical  $s$  process [1] is influenced by the competition between radiative neutron capture and  $\beta$ -decay processes for many nuclei with half-lives ranging from weeks to years. The  $(n, \gamma)$  cross sections for these nuclei are required to uncover the properties of these astrophysical environments from observed isotopic abundances [2]. Evaluations of nuclear-reactor system designs and fuel-cycle concepts require neutron-capture cross sections on short-lived actinides. In addition, accurate  $(n, \gamma)$  cross-section measurements are needed for a variety of applications in homeland security and stockpile stewardship.

For many short-lived nuclei, indirect methods are the only foreseeable way to determine these cross sections. The surrogate nuclear reaction method [3,4] can be used to determine cross sections for compound-nuclear reactions using a combination of reaction modeling and experimental results. The method involves creating the desired compound nucleus through a different (“surrogate”) reaction that involves a more experimentally accessible combination of projectile and target. This approach was first used in the 1970’s to extract  $(n, f)$  cross sections for various actinides from transfer reactions with  $t$  and  $^3\text{He}$  projectiles on neighboring (long-lived) nuclei, followed by fission [5,6]. Recently, the technique was applied to determine  $(n, f)$  cross sections at neutron energies up to 20 MeV for actinide nuclei using a variety of light-ion reactions [7–12]. At energies below  $\sim 1$  MeV, theoretical studies indicated that mismatches in the compound-nucleus spin-parity distributions between the neutron-induced and surrogate reactions can affect the interpretation of a surrogate measurement

[3] and therefore cannot be neglected. For  $(n, f)$  cross sections, these issues were recently considered in Refs. [13,14].

For  $(n, \gamma)$  cross sections, the results of the surrogate technique are even more likely to be sensitive to spin ( $J$ ) and parity ( $\pi$ ) differences between neutron-induced and surrogate reactions [15,16]. Recent surrogate analyses for rare-earth [17,18] and actinide [19,20] nuclei were carried out assuming that these  $J^\pi$  differences are small enough that they do not cause significant systematic shifts. While the results appear roughly consistent with existing direct measurements, the experimental uncertainties are large.

In the work reported here, the validity and limitations of some of the methods that were recently used to extract  $(n, \gamma)$  cross sections from surrogate nuclear reactions are explored. Inelastic proton scattering experiments were carried out on  $^{154,156,158}\text{Gd}$  nuclei, which, in principle, can be used to determine  $^{153,155,157}\text{Gd}(n, \gamma)$  cross sections for neutron energies up to 3 MeV. These isotope choices allow a comparison of the results of the approximate surrogate methods with high-quality direct  $(n, \gamma)$  cross-section measurements [21,22]. Particular attention is paid to effects that arise from the  $J^\pi$  mismatch between desired and surrogate reactions. These comparisons, along with Hauser-Feshbach-type calculations of the surrogate reactions, provide insights into the limitations of the approximations studied and allow the formulation of recommendations for future experiments.

## II. SURROGATE NUCLEAR REACTION TECHNIQUE FOR NEUTRON CAPTURE

The surrogate nuclear reaction method can be used to indirectly determine cross sections of two-step nuclear reactions

that proceed through a highly excited, equilibrated compound nucleus. A brief description of the method is presented here: For more detailed discussions, see Refs. [3,15].

In Hauser-Feshbach theory [23],  $(n, \gamma)$  cross sections  $\sigma_{n\gamma}^{\text{HF}}(E_n)$  can be expressed in terms of the cross section  $\sigma_n^{\text{CN}}(E_n)$  for the formation of the compound nucleus at neutron energy  $E_n$  and the exit-channel branching ratio  $G_\gamma^{\text{CN}}(E_{\text{ex}})$  for  $\gamma$ -ray decay through the relation

$$\sigma_{n\gamma}^{\text{HF}}(E_n) = \sum_{J,\pi} \sigma_n^{\text{CN}}(E_n, J, \pi) G_\gamma^{\text{CN}}(E_{\text{ex}}, J, \pi). \quad (1)$$

Here  $E_{\text{ex}}$  denotes the excitation energy of the decaying compound nucleus; it is related to the neutron energy  $E_n$  via

$$E_n = \frac{A+1}{A}(E_{\text{ex}} - S_n), \quad (2)$$

where the near-unity factor  $(A+1)/A$  accounts for the nuclear-recoil energy imparted in the neutron-induced reaction on a nucleus consisting of  $A$  nucleons. In Eq. (1), width-fluctuation correlations between incident and outgoing channels (typically included in applications of Hauser-Feshbach theory) were neglected. Note that, in general,  $\sigma_n^{\text{CN}}$  and  $G_\gamma^{\text{CN}}$  are expected to depend on both the spin  $J$  and parity  $\pi$  of the compound-nuclear system. Although the  $\sigma_n^{\text{CN}}$  cross sections can, in many cases, be accurately determined using optical models, the exit-channel probabilities are often difficult to calculate reliably, as they require detailed information on level densities, strength functions, and other nuclear properties of the various decay channels. However, the decay pattern of the compound nucleus can be experimentally studied using a surrogate nuclear reaction. The desired compound nucleus is produced at the energies of interest (albeit with possibly a different  $J^\pi$  distribution) using an alternative (or “surrogate”) reaction. This surrogate reaction is typically chosen so that it involves a *light-ion* reaction on a *stable* (or more readily accessible) target.

In the surrogate reaction, the measured decay probability  $P_{\delta\gamma}$ , depends on  $G_\gamma^{\text{CN}}$  from Eq. (1) through the relation

$$P_{\delta\gamma}(E_{\text{ex}}) = \sum_{J,\pi} F_\delta^{\text{CN}}(E_{\text{ex}}, J, \pi) G_\gamma^{\text{CN}}(E_{\text{ex}}, J, \pi), \quad (3)$$

where  $F_\delta^{\text{CN}}$  are the direct-reaction probabilities that, in general, must be calculated and  $\delta$  indicates the direct-reaction channel that leads to the formation of the compound nucleus. The goal of the surrogate approach is to use the measured  $P_{\delta\gamma}$ , together with the calculated  $F_\delta^{\text{CN}}(E_{\text{ex}}, J, \pi)$ , to determine (or constrain) the branching ratios  $G_\gamma^{\text{CN}}(E_{\text{ex}}, J, \pi)$ , so that the desired cross section can be determined with Eq. (1).

While the full surrogate formalism takes into account angular-momentum and parity considerations, surrogate experiments are often analyzed using approximations. In particular, most applications of the surrogate method invoke the Weisskopf-Ewing (WE) limit of the Hauser-Feshbach theory [24] and assume that the branching ratios  $G_\gamma^{\text{CN}}$  are independent

of  $J^\pi$ . In this limit, Eq. (1) simplifies to

$$\sigma_{n\gamma}^{\text{HF}}(E_n) = \sigma_n^{\text{CN}}(E_n) G_\gamma^{\text{CN}}(E_{\text{ex}}), \quad (4)$$

and  $P_{\delta\gamma}(E_{\text{ex}}) = G_\gamma^{\text{CN}}(E_{\text{ex}})$ .

A variety of recent experiments [7–9,11–14] and theoretical studies [3] showed that the WE approximation seems to work well for extracting  $(n, f)$  cross sections for neutron energies  $\gtrsim 1$  MeV from surrogate measurements. However, its validity for  $(n, \gamma)$  applications is still under investigation. In fact, theoretical studies indicate that  $J^\pi$  differences between the desired and surrogate reactions can have a significant impact on the interpretation of a surrogate measurement [4,15,16]. In extreme cases where the decay of the compound nucleus is dominated by transitions to discrete levels in neighboring nuclei, such as in the region near  $^{90}\text{Zr}$ , the  $(n, \gamma)$  cross section inferred using the WE approximation can be off by an order of magnitude [15]. Although the sensitivity to the  $J^\pi$  difference is expected to be much less dramatic in regions with deformed nuclei, it is not obvious that angular momentum effects can ever be ignored for a reliable determination of a  $(n, \gamma)$  cross section.

The application of the surrogate nuclear reaction method to  $(n, \gamma)$  cross sections poses the additional challenge of obtaining high-quality experimental data. The signature of the exit channel is a complex  $\gamma$ -ray cascade from a highly excited compound nucleus. No single  $\gamma$  ray is emitted in all decays and electron conversion can obscure low-energy transitions. Compared to fission-fragment detection,  $\gamma$ -ray spectroscopy is typically less efficient and prone to backgrounds from the neutron-emission exit channel and impurities in the target. For example, target impurities (even if only at the percent level) can introduce significant backgrounds because the  $\gamma$ -ray exit channel decreases rapidly with energy and therefore can be orders of magnitude smaller than the cross section for unwanted nuclear reactions that occur within the target material. In addition, the interest in low-energy cross sections means the excitation energy of the compound nucleus must be determined accurately and with excellent energy resolution to avoid obscuring the energy dependence of the cross section and to ensure that events from energies below  $S_n$  do not compromise the data.

The Gd region is well suited for tests of the surrogate nuclear reaction method because many stable Gd isotopes exist for which  $(n, \gamma)$  cross sections were directly measured and sufficient nuclear structure information is available to carry out complementary cross-section calculations. For deformed Gd nuclei, the level densities at low excitation energies are much higher than for the near-spherical nuclei considered in Ref. [15] and thus the decay probabilities are expected to depend less sensitively on compound-nuclear  $J^\pi$  distributions and on details of low-energy nuclear structure. For the  $^{155,157}\text{Gd}$  isotopes,  $(n, \gamma)$  cross sections were directly measured up to 0.8–1.0 MeV with typical uncertainties below 1% [21] and at 0.5, 1.0, and 2.5 MeV with uncertainties of  $\approx 10\%$  [22]. The two sets of measurements agree in the region of overlap. In addition, the compound-nuclear  $J^\pi$  distributions for all the reactions are expected to be nearly identical because the ground state  $J^\pi$  of  $^{153,155,157}\text{Gd}$  and  $^{154,156,158}\text{Gd}$  are all  $3/2^-$  and  $0^+$ , respectively.

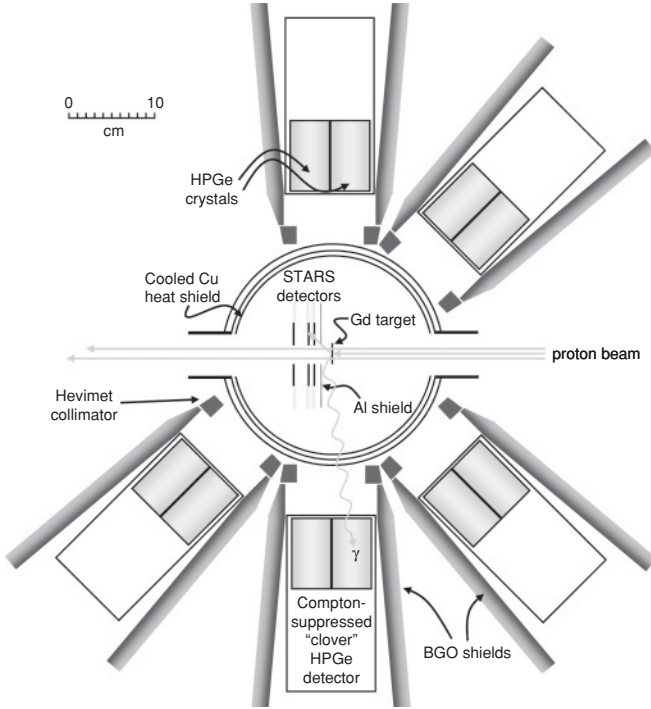


FIG. 1. Layout of the experimental setup. Protons from the 88-Inch Cyclotron bombarded Gd targets held at the center of the vacuum chamber. Scattered protons were detected using STARS operated in a  $\Delta E$ - $E1$ - $E2$  configuration. The interior of the chamber was lined with a cooled copper heat shield to reduce the thermal noise of the particle detectors. The LiBerACE HPGe detectors detected  $\gamma$  rays in coincidence with scattered protons.

### III. EXPERIMENT

Inelastic scattering reactions on  $^{154,156,158}\text{Gd}$  nuclei served as the surrogate reaction for the  $^{153,155,157}\text{Gd}(n,\gamma)$  reactions. The experimental setup is shown in Fig. 1. The apparatus is described in depth in Ref. [25]. Gadolinium targets were bombarded with  $\approx 2$  nA of 22-MeV protons from the 88-Inch Cyclotron at the Lawrence Berkeley National Laboratory. Scattered protons were detected using the Silicon Telescope Array for Reaction Studies (STARS) arranged in a  $\Delta E$ - $E1$ - $E2$  configuration [25,26]. Protons were selected as the light-ion beam for the following reasons: (a) The excitation energy can be measured with good energy resolution, (b) the Si detectors can be reliably calibrated using standard  $\alpha$  sources and *in situ* proton scattering data from discrete states of  $^{12}\text{C}$  and  $^{16}\text{O}$  (as explained in Sec. III B), and (c) kinematic and dead-layer energy-loss corrections were minimized.

The excitation energy of a struck nucleus following proton scattering is determined from

$$E_{\text{ex}} = E_b - E_p - E_r, \quad (5)$$

where  $E_b$  is the energy of the incident proton beam,  $E_p$  is the scattered proton energy (corrected for energy loss in apparatus dead layers), and  $E_r$  is the recoil energy imparted to the nucleus. To detect  $\gamma$  rays in coincidence with scattered protons, the target chamber and STARS array were surrounded by the Livermore-Berkeley Array for Collaborative Experiments

(LiBerACE), which, in this experiment, consisted of five clover-type high purity germanium (HPGe) detectors [27] with bismuth-germanate-oxide (BGO) Compton-suppression shields [28]. Detection of characteristic  $\gamma$  rays from ground-state band transitions of the even-even  $^{154,156,158}\text{Gd}$  nuclei identified ( $p, p\gamma$ ) reactions.

The probability that the nucleus de-excites by  $\gamma$ -ray emission  $P_{\delta\gamma}$  was determined from the relation

$$P_{\delta\gamma}(E_{\text{ex}}) = \frac{(1 + \alpha_{\text{IC}})}{\epsilon_\gamma f(E_{\text{ex}})} \times \frac{N_{\delta\gamma}(E_{\text{ex}})}{N_\delta(E_{\text{ex}})}, \quad (6)$$

where  $N_{\delta\gamma}$  and  $N_\delta$  were the number of detected  $p$ - $\gamma$  coincidences and scattered protons, respectively,  $f$  is the energy-dependent fraction of  $\gamma$ -ray cascades that pass through the transition of interest, and  $\epsilon_\gamma$  and  $\alpha_{\text{IC}}$  were the  $\gamma$ -ray detection efficiency and internal conversion coefficient for this transition. The proton detection efficiency cancels in the ratio.

Two hardware triggers selected events to record to determine  $N_\delta$  and  $N_{\delta\gamma}$ . For  $N_\delta$ , a “particle singles” trigger selected events with pulses above threshold in at least one ring and one sector of both the  $\Delta E$  and  $E1$  Si detectors. This trigger was downscaled (only every 50th event was recorded to disk) to limit acquisition dead time. A “particle- $\gamma$  coincidence” trigger was generated when the “particle singles” trigger was within 4  $\mu\text{s}$  of any  $\gamma$  ray detected by a LiBerACE HPGe detector. These data were used to determine  $N_{\delta\gamma}$ .

#### A. Gd targets

Properties of the isotopically enriched, self-supporting  $^{154,156,158}\text{Gd}$  metal foil targets are listed in Table I. The  $^{154}\text{Gd}$  target was the only target with an enrichment less than 90%. In each case, the remainder consisted primarily of other Gd isotopes. Target composition was determined by the supplier using spark-source mass spectrometry [29]. The only other element detected was Eu at a level of 0.2%. The targets were handled in dry-N environments prior to installation in the vacuum system to minimize oxidation. Nonetheless, signatures of H, C, and O contamination were apparent in the data. These contaminants were likely introduced during target fabrication and handling.

The  $^{154}\text{Gd}$  target contained a significant fraction (17.5%) of  $^{155}\text{Gd}$ . Unfortunately,  $^{155}\text{Gd}(p, pn)^{154}\text{Gd}$  reactions yield

TABLE I. Properties of Gd targets and ground-state  $E2$   $\gamma$ -ray transitions used in this measurement.

Property	$^{154}\text{Gd}$	$^{156}\text{Gd}$	$^{158}\text{Gd}$
Thickness [mg/cm <sup>2</sup> ]	1.01(10)	0.90(9)	1.01(10)
Isotopic Purity [%]	66.53(10)	93.79(3)	92.00(10)
$A^{+1}\text{Gd}$ Content [%]	17.50(10)	2.53(2)	0.00
$S_n$ [keV]	8894.71(17)	8536.39(7)	7937.39(6)
$E_{2^+ \rightarrow 0^+}$ [keV]	123.0706(9)	88.970(1)	79.513(2)
$E_{4^+ \rightarrow 2^+}$ [keV]	247.9288(7)	199.2190(1)	181.943(1)
$E_{6^+ \rightarrow 4^+}$ [keV]	346.643(5)	296.532(3)	277.554(8)
$E_{8^+ \rightarrow 6^+}$ [keV]	426.78(7)	380.417(5)	365.10(3)

the same characteristic  $\gamma$  rays as ( $p, p'$ ) scattering on  $^{154}\text{Gd}$ . Therefore, data were collected with an enriched  $^{155}\text{Gd}$  target to subtract off this background contribution. For the  $^{156}\text{Gd}$  target data set, this correction was small ( $^{157}\text{Gd}$  fraction was only 2.53%) and was estimated from the 3.56%  $^{157}\text{Gd}$  contamination in the  $^{158}\text{Gd}$  target. No correction was required for  $^{158}\text{Gd}$  because  $^{159}\text{Gd}$  is short-lived ( $t_{1/2} < 1$  day).

Each target was  $\approx 1$  mg/cm<sup>2</sup> thick with a uniformity of 10% quoted by the supplier [29]. The target thicknesses were verified by determining the energy lost by  $\alpha$  particles passing through the target using a simple setup consisting of a  $^{226}\text{Ra}$  source and a segmented Si detector. The results of these measurements were consistent with the quoted thicknesses and uniformities.

### B. Particle detection

The STARS detectors consisted of three highly segmented, double-sided Si  $S2$  detectors [30] in a  $\Delta E$ - $E1$ - $E2$  telescope configuration. The  $\Delta E$  detector was 500  $\mu\text{m}$  thick and segmented into 48 rings (each 0.5 mm wide) and 16 sectors (each spanning 22.5°). The  $E1$  and  $E2$  detectors were each 1000  $\mu\text{m}$  thick and operated with a 2 times coarser segmentation of 24 rings and 8 sectors. A 200  $\mu\text{g}/\text{cm}^2$  thick aluminum foil in front of the Si stopped low-energy  $\delta$  electrons that emerged from the target that can degrade the detector performance. A copper heat shield surrounded the detector array and was cooled by continuously flowing chilled ethylene glycol through a channel in its frame. Maintaining the ethylene glycol at 0°C lowered the detector temperature to 15°C to reduce thermal noise.

The signal readout is described in detail in Ref. [8]. The charge collected from the  $p$  (ring) and  $n$  (sector) sides determined the energy deposition and hit location for each detector. Only events with energy deposited in a single sector and a single cluster of consecutive rings were selected for analysis. The energy deduced from the ring and the sector sides were required to agree to within 400 keV. For the  $\Delta E$  detector, ring and sector response had comparable energy resolution, so the average of the two was used. For the  $E1$  detector, cross-talk between neighboring rings was evident and (even after correcting for this effect) degraded the resolution obtainable from the rings. For the  $E2$  detector, the ring performance was limited by low-resolution electronics. Therefore, for both the  $E1$  and  $E2$  detectors, the energy was determined solely from the sectors.

The response of each ring and sector of the three detectors was calibrated using a  $^{226}\text{Ra}$   $\alpha$  source ( $\alpha$  lines used in decay chain:  $E_\alpha = 4784.34(25)$ ,  $5304.33(7)$ ,  $5489.48(30)$ ,  $6002.35(9)$ , and  $7686.82(7)$  keV [31]) after the online data collection. The typical  $1\sigma$  intrinsic resolution was  $\approx 20$  keV. The calibration was adjusted by 0.34% when applied to proton data because of the estimated difference in the pulse-height defect [32]. Most detected protons deposited between 3 to 14 MeV in individual detectors. Therefore, this calibration did not need to be extrapolated more than 7 MeV. The  $\Delta E$  and  $E2$  detectors were calibrated in place without disturbing the silicon telescope. Calibration of the  $E1$  detector, which was sandwiched between the other two detectors, required

dismantling the telescope and the gain was expected to be affected by the handling. It was found that to be consistent with *in situ* measurements, the detector calibration had to be scaled by  $\approx 2\%$  (see discussion in the following).

Energy loss in traversing the target and dead layers in the apparatus (200  $\mu\text{g}/\text{cm}^2$  aluminum shield in front of the telescope and detector surface metallizations of 30  $\mu\text{g}/\text{cm}^2$  Al or 580  $\mu\text{g}/\text{cm}^2$  Au [30] depending on orientation) was accounted for on an event-by-event basis for both calibrations and online data. The  $1/\cos\theta$  angular dependence (impact angle  $\theta$  was determined from the known geometry based on the ring struck) of the energy loss observed in the sector energy measurements were consistent with the expected dead layers.

Charged particles were identified from the energy deposited in  $\Delta E$  ( $E_\Delta$ ) and  $E1$  ( $E_1$ ) detectors from their characteristic values of

$$a = \frac{\cos\theta}{T} \left( (E_\Delta + E_1)^{1.75} - E_1^{1.75} \right), \quad (7)$$

where  $\frac{T}{\cos\theta}$  is the path length through the  $\Delta E$  detector of thickness  $T$ . This relation is based on the empirically determined range of particles in a matter of  $a^{-1}E^{1.75}$ , where  $a$  is a constant that scales with the rate of energy loss [33]. The identification of protons, deuterons, and tritons from  $a$  is shown in Fig. 2. All other isotopes (and most of the tritons) are stopped in the 500- $\mu\text{m}$  thick  $\Delta E$  detector.

The experiment was optimized to detect scattered protons with energies 10–17 MeV (corresponding to excitation energies of 5–12 MeV). Protons with energies less than about 10 MeV were stopped in the  $\Delta E$  detector and therefore did not provide a trigger for the data acquisition. Above 17 MeV, most protons were not stopped by the  $\Delta E$  and  $E1$  detectors. These protons had significant angular straggling as they emerged from the back of the  $E1$  detector and only a fraction hit the  $E2$  detector, which was spaced an additional 1 cm further back to accommodate signal cables. These events were not of interest

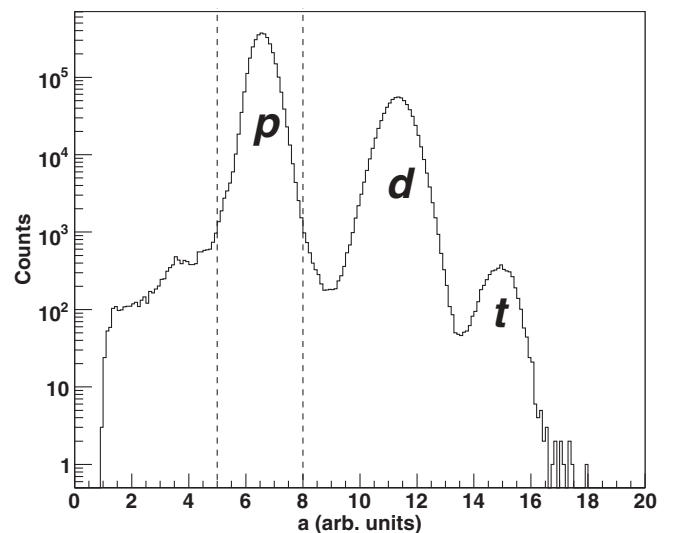


FIG. 2. Charged particle identification from energy loss for particles stopped in  $\Delta E$ - $E1$  Si telescope. Only protons, deuterons, and tritons were observed. The particles between the dashed lines were selected for this work.

because they corresponded to excitation energies  $<5$  MeV, well below the Gd neutron separation energies (8–9 MeV). Any event with energy detected in the  $E2$  detector was discarded.

The scattering direction was determined from the vector connecting the beam spot at the target to the struck  $\Delta E$  detector element. This allowed event-by-event reconstruction of the kinetic energy imparted to struck nuclei. To ensure that only particles originating from the target foil (with radius 9.5 mm) were accepted, the vector constructed by connecting the spatial hit patterns of the  $\Delta E$  and  $E1$  detectors was traced back and required to intersect the target plane within 8 mm of the center.

For Gd, the recoil energy  $E_r$  imparted was roughly 100 keV, while for the lighter  $^{12}\text{C}$  and  $^{16}\text{O}$  contaminants in the target,  $E_r$  was 0.7–1.5 MeV, and for  $^1\text{H}$  it can be  $\sim 10$  MeV. The sensitivity of  $E_r$  for  $^1\text{H}$ ,  $^{12}\text{C}$ , and  $^{16}\text{O}$  was exploited to precisely determine the beam, target, and detector geometry. For Eq. (5) to hold for the measured  $^1\text{H}$  elastic scattering peak, the target-to-detector distance must have been  $18.9 \pm 0.2$  mm. This value agreed with, and was more precise than, direct vernier caliper measurements of  $18.5 \pm 1.0$  mm. The resolution of the  $^1\text{H}$  elastic peak implied that the cyclotron beam spot full-width at half maximum (FWHM) was  $\lesssim 1.7$  mm. The beam spot was determined to be  $1.2 \pm 0.2$  mm off-center based on differences in  $E_r$  for each sector inferred from inelastic scattering off of discrete states in  $^{12}\text{C}$  and  $^{16}\text{O}$ . No change in any of these beam parameters was observed over the course of data collection.

With the experimental geometry precisely known, the uncertainty in the recoil corrections was  $\pm 10$  keV for  $^{12}\text{C}$  and  $^{16}\text{O}$  and  $\pm 1$  keV for the Gd isotopes. Scattering from discrete states in these isotopes was used as an *in situ* energy calibration. The energy of these peaks was found to differ from the known values when the  $^{226}\text{Ra}$  calibrations (corrected for pulse-height defect) were used for all three detectors. This was interpreted as a shift in the response of the  $E1$  detector resulting from the dismantling of the telescope and implied the calibration of this detector had to be adjusted by 2.6%. After applying this correction, the measured proton energies  $E_p$  for scattering off of  $^{12}\text{C}$  and  $^{16}\text{O}$  nuclear states at energy  $E_s$  agreed with  $E_b - E_s - E_r$  to within  $\pm 50$  keV as can be seen in Fig. 3. Therefore, 50 keV was considered a conservative estimate of the uncertainty in reconstructed proton energy over the entire energy range. Using this energy calibration, the cyclotron beam energy was determined to be  $E_b = 21.70 \pm 0.05$  MeV, which is consistent (within the 2% machine calibration uncertainty [34]) with the 22 MeV requested. In addition, the  $1\sigma$  width of the elastic peak was measured to be 65 keV. The excitation energy was assumed to be determined with this resolution.

### C. $\gamma$ -ray detection

Calibrations of the 19 clover crystals (one crystal was not analyzed due to poor resolution) were performed immediately following the end of data collection. The energy scale was determined from second-order polynomial fits to lines from  $^{152}\text{Eu}$  and  $^{56}\text{Co}$  decay. Applying this calibration to known Gd transitions observed online revealed a gain shift in about half the crystals by  $\approx 0.2\%$  between data collection and detector calibration. When these drifts were removed, the response of

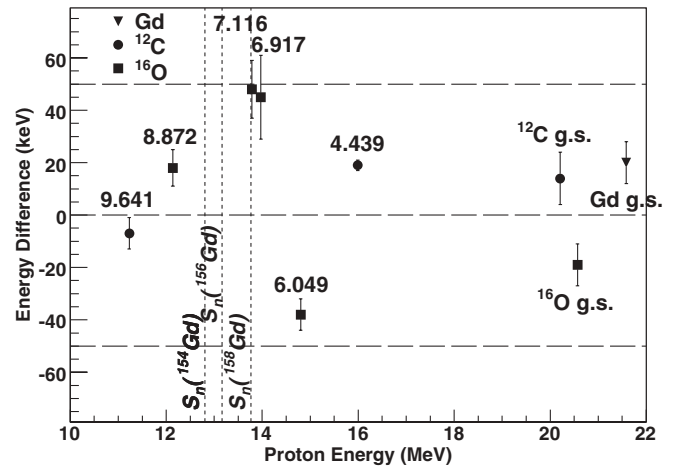


FIG. 3. Difference between known proton energies and energies measured using the STARS telescope. The low-lying discrete states in  $^{12}\text{C}$  and  $^{16}\text{O}$  (with energies listed in MeV above the points) provide an *in situ* calibration over the energy range of interest. The kinetic energy imparted to the struck nucleus is not observed, but can be calculated based on kinematics. The error bars shown are statistical only. At each point, the agreement is within  $\pm 50$  keV and this is taken as the energy uncertainty. The dashed vertical lines show the proton energy that corresponds to  $S_n$  for each Gd isotope.

all the detectors were aligned to within 0.2 keV at ground-state band transitions and within 1 keV at energies  $>1000$  keV. The spectra from all the detectors were summed together and the resulting resolution (FWHM) of 1.8 keV at 300 keV and 2.7 keV at 1000 keV was nearly identical to the resolution of the individual crystals.

The energy-dependent efficiency  $\epsilon_\gamma(E_\gamma)$  of the LiBerACE detectors was determined offline using calibrated  $^{152}\text{Eu}$ ,  $^{133}\text{Ba}$ , and  $^{207}\text{Bi}$  sealed sources placed at the target location. Additional efficiency calibrations were performed *in situ* by analyzing  $p$ - $\gamma$ - $\gamma$  coincidences in  $6^+ \rightarrow 4^+ \rightarrow 2^+$  and  $4^+ \rightarrow 2^+ \rightarrow 0^+$  ground-state band cascades of  $^{154,156,158}\text{Gd}$  nuclei. Detection of the  $\gamma$  ray from the higher-lying state, denoted  $\gamma_1$ , signaled the nearly simultaneous emission of either a second  $\gamma$  ray,  $\gamma_2$ , or a conversion electron (with probabilities dependent on the calculated conversion coefficient  $\alpha_2$ ). The efficiency  $\epsilon_2$ , for detecting  $\gamma_2$ , was determined from the ratio of the number of  $\gamma_1$ - $\gamma_2$  coincidences,  $N_{\gamma_2\gamma_1}$ , relative to the total number of  $\gamma_1$  events observed,  $N_{\gamma_1}$ , after including small ( $\sim 5\%$ ) corrections

$$\epsilon_2 \approx \frac{N_{\gamma_2\gamma_1}}{N_{\gamma_1}} \times (1 + \alpha_2) \times \frac{n}{n-1} \times (1 + \Omega_C). \quad (8)$$

Here  $n = 19$  is the number of HPGe detector crystals so  $\frac{n-1}{n}$  is the fraction of detectors available to detect  $\gamma_2$  following the detection of  $\gamma_1$  (assuming all elements have identical detection efficiency). Summing corrections were negligible because each detector element subtended only 0.3% of  $4\pi$ .  $\Omega_C$  allows for a change in efficiency due to  $\gamma$ - $\gamma$  angular correlations. This term is  $<0.04$  even for large correlations because of the substantial in-plane coverage of the array.

The results of these calibrations are shown in Fig. 4. No addback routine is used. The efficiency of the array

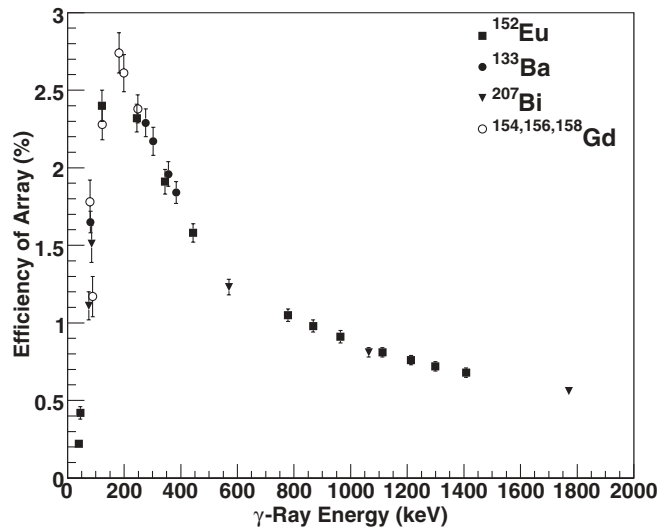


FIG. 4. The efficiency of the LiBerACE HPGe array determined using  $^{152}\text{Eu}$ ,  $^{133}\text{Ba}$ , and  $^{207}\text{Bi}$  sealed sources and transitions in  $^{154,156,158}\text{Gd}$  measured *in situ*.

peaks at 2.7% for  $\gamma$  rays of  $\approx 180$  keV. Above this energy, the uncertainty is 5% and below this the uncertainty is approximately 10–15%.

Internal conversion coefficients ( $\alpha_{IC}$ ) were calculated using the software BRICC V. 2.0B [35], which is based on relativistic self-consistent Dirac-Fock calculations that take into account the atomic vacancy created during the conversion process. The authors estimate an uncertainty of  $\pm 1.4\%$  for the accuracy of calculated coefficients.

## IV. RESULTS

### A. $\gamma$ -ray exit-channel probability

Figure 5 shows the measured  $\gamma$ -ray spectra from all the data collected with excitation energies below  $S_n$ . The most prominent  $E2$  transitions from the  $8^+$ ,  $6^+$ ,  $4^+$ , and  $2^+$  states of the ground-state band were used to determine  $N_{\delta\gamma}$ . Using these spectra, the response (Gaussian centroid and width) of the LiBerACE detectors were determined at the lines of interest. These properties were fixed for all subsequent curve fitting (at energies both above and below  $S_n$ ) involving these transitions. At excitation energies above  $S_n$ ,  $P_{\delta\gamma} < 1$  because of competition from neutron emission. To determine  $N_{\delta\gamma}$  as a function of  $E_{ex}$ , the data were sorted into 100 keV excitation energy bins. In each bin, the  $\gamma$ -ray spectrum was fit to a Gaussian peak with a fixed centroid and width on top of a linear background to determine the number of counts in the transitions of interest. Typical fitting ranges covered  $\gamma$ -ray energies of 20 keV centered on the line to constrain the background (for a few transitions the range was truncated because of a nearby line). For energies below  $S_n$ , the background was nearly linear with no notable structure. Above  $S_n$ ,  $\gamma$ -ray lines from  $(p,pn)$  reactions were observed. The amplitudes of any known transitions within the fitting range that can be emitted following  $n$  emission from the target nucleus (statistical or otherwise) were included as free parameters with the widths fixed to that of the nearby

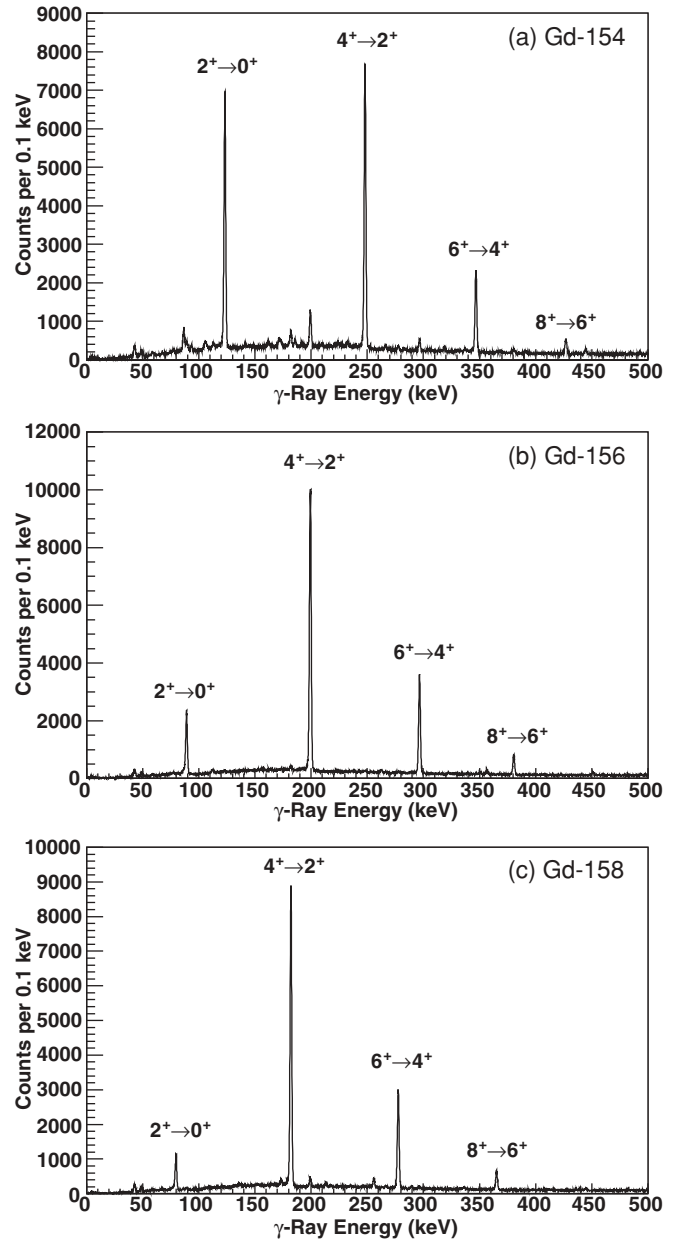


FIG. 5. The  $\gamma$ -ray spectra for (a)  $^{154}\text{Gd}$ , (b)  $^{156}\text{Gd}$ , and (c)  $^{158}\text{Gd}$  when  $E_{ex} < S_n$ . The  $E2$  transitions of interest had high statistics, favorable signal-to-background, and no contamination from  $\gamma$  rays associated with  $(p,pn)$  reactions. These spectra were used to determine the HPGe detector response at these transitions for reactions with  $E_{ex} > S_n$ .

line of interest and the centroid fixed by the known energy difference. Only for the  $2^+ \rightarrow 0^+$  transition at 79.5 keV in  $^{158}\text{Gd}$  was this an important consideration. In this case, a nearby  $7/2^- \rightarrow 5/2^-$  transition at 76.9 keV in  $^{157}\text{Gd}$  was a significant background above  $S_n$ .

The number of inelastic scattering events observed off of the Gd isotope of interest  $N_\delta$  was determined from the proton-singles data. Due to limitations in target enrichment and purity, contributions from contaminants and other Gd isotopes had to be measured and subtracted. The measured proton

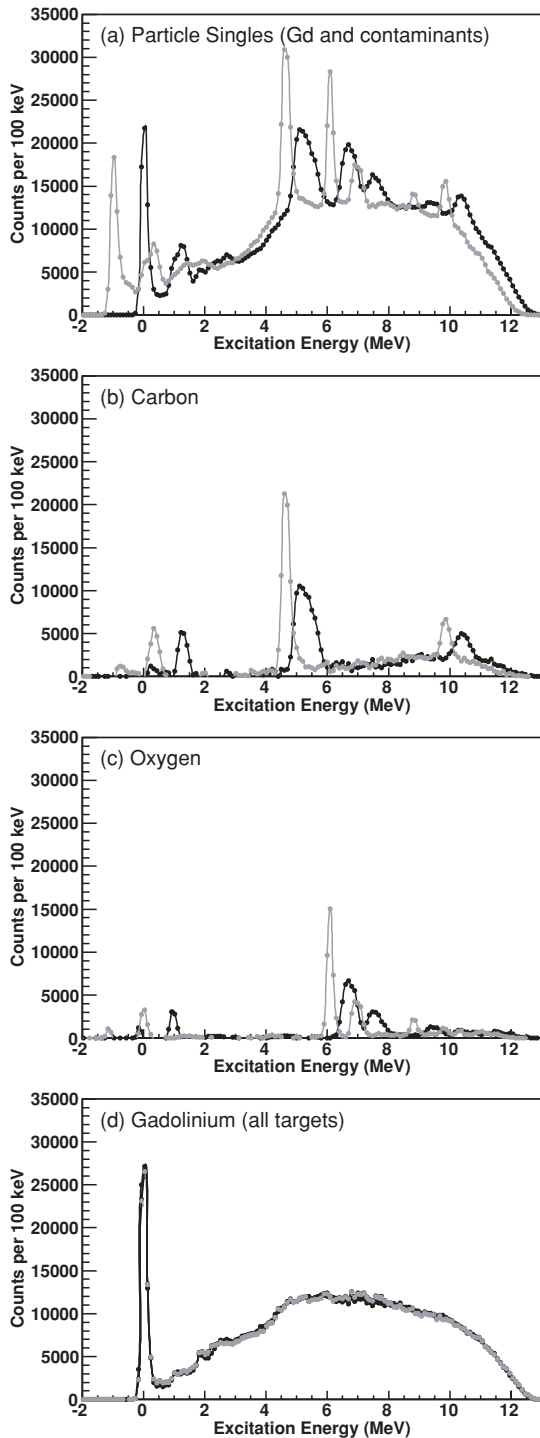


FIG. 6. Particle-singles data with excitation energies corrected for nuclear recoil based on the kinematics of striking Gd (black) and  $^{16}\text{O}$  (grey) nuclei. In (a) are the results for the  $^{156}\text{Gd}$  target. After taking linear combinations of the four targets, which each had differing levels of C and O contamination, the spectrum for (b) C, (c) O, and (d) Gd can be isolated.

singles spectrum from the  $^{156}\text{Gd}$  target is shown in Fig. 6(a) and the observed structure is typical of all the targets. Some of this structure is due to scattering from the ground and excited states in C and O. When the excitation energy is determined using

the recoil energy  $E_r$  for the appropriate mass, the width of the peaks became comparable to the telescope energy resolution inferred from the elastic scattering peak. Differing levels of hydrocarbon and oxidative contamination for each target was evidence from the magnitude of these peaks. Discrete lines from other contaminants were not observed in any of the targets.

The separate contributions from these contaminants were isolated by taking appropriate linear combinations of the spectra from the four targets to eliminate the most prominent peaks. The results are shown in Fig. 6(b) through 6(d) corrected for both the kinetic energy imparted to Gd and  $^{16}\text{O}$  nuclei. Several excited states of  $^{12}\text{C}$  and  $^{16}\text{O}$  can be clearly identified. The shape of the Gd spectra is primarily due to the acceptance of the detection scheme.

For the  $^{154}\text{Gd}$  target,  $(p, pn)$  reactions on  $^{155}\text{Gd}$  yielded the characteristic  $\gamma$  rays of interest at excitation energies greater than  $S_n(^{155}\text{Gd}) = 6.435$  MeV. Data collected with an enriched  $^{155}\text{Gd}$  target was used to subtract this background. In principle, the magnitude of the background subtraction can be determined from the relative isotopic compositions (from the supplier), target thicknesses, and measured integrated beam current. However, the target thickness uncertainties were  $\approx 10\%$ . Instead, a precision of 2% was obtained by using the relative number of detected 46-keV Gd x-rays to determine the ratio of target thicknesses and beam currents. The appropriate scaling for the background subtraction was also determined from the relative number of observed  $\gamma$  rays due to other reactions on  $^{155}\text{Gd}$ . The relative number of  $7/2_1^- \rightarrow 5/2_1^-$  and  $9/2_1^- \rightarrow 7/2_1^-$  transitions in  $^{155}\text{Gd}$  from  $(p, p')$  scattering and the  $^{154}\text{Gd}$  ground-state band transitions from  $(p, d)$  reactions had the best statistics and signal-to-background. The scaling determined by each of these methods were consistent. The  $^{157}\text{Gd}(p, pn)$  background in the  $^{156}\text{Gd}$  measurement was determined from the characteristic  $\gamma$  rays from the decay of  $^{156}\text{Gd}$  excited states from the small sample of  $^{157}\text{Gd}$  in the enriched  $^{158}\text{Gd}$  target.

After subtracting the  $(p, pn)$  backgrounds for  $^{154}\text{Gd}$  and  $^{156}\text{Gd}$ , the results for  $P_{\delta\gamma}$  for the compound nuclei were determined from Eq. (6). For each of the ground-state band transitions, the  $\gamma$ -ray exit-channel probability is nearly independent of energy below  $S_n$  and dropped rapidly above  $S_n$  as expected. Below  $S_n$ ,  $\gamma$ -ray emission (including electron conversion) is the only open channel so  $P_{\delta\gamma}$  must equal unity. The unknown fraction  $f$  of cascades that pass through the particular transition of interest was set to the value required to make  $P_{\delta\gamma} = 1$  in Eq. (6) for the data collected with excitation energies extending from 5 MeV to  $S_n$ . It was found that  $f$  varied slightly with energy and can be represented by  $f(E_{\text{ex}}) = f_0[1 + b(E_{\text{ex}} - S_n)]$  where the values  $f_0$  and  $b$  depended on the transition but not the isotope. For the  $2^+ \rightarrow 0^+$  transition,  $f_0 \approx 0.9$  demonstrating that it is part of most  $\gamma$ -ray cascades as expected. The term  $b$ , which determined the size of energy dependence ranged from  $(-0.03 \pm 0.02)$  per MeV for the  $2^+ \rightarrow 0^+$  transition to  $(+0.04 \pm 0.04)$  per MeV for the  $8^+ \rightarrow 6^+$  transition. These  $f(E_{\text{ex}})$  functions determined below  $S_n$  were used to determine  $P_{\delta\gamma}$  at all excitation energies.

The resulting  $P_{\delta\gamma}$  are shown in Fig. 7 for the four lowest ground-state band transitions. The overall uncertainty



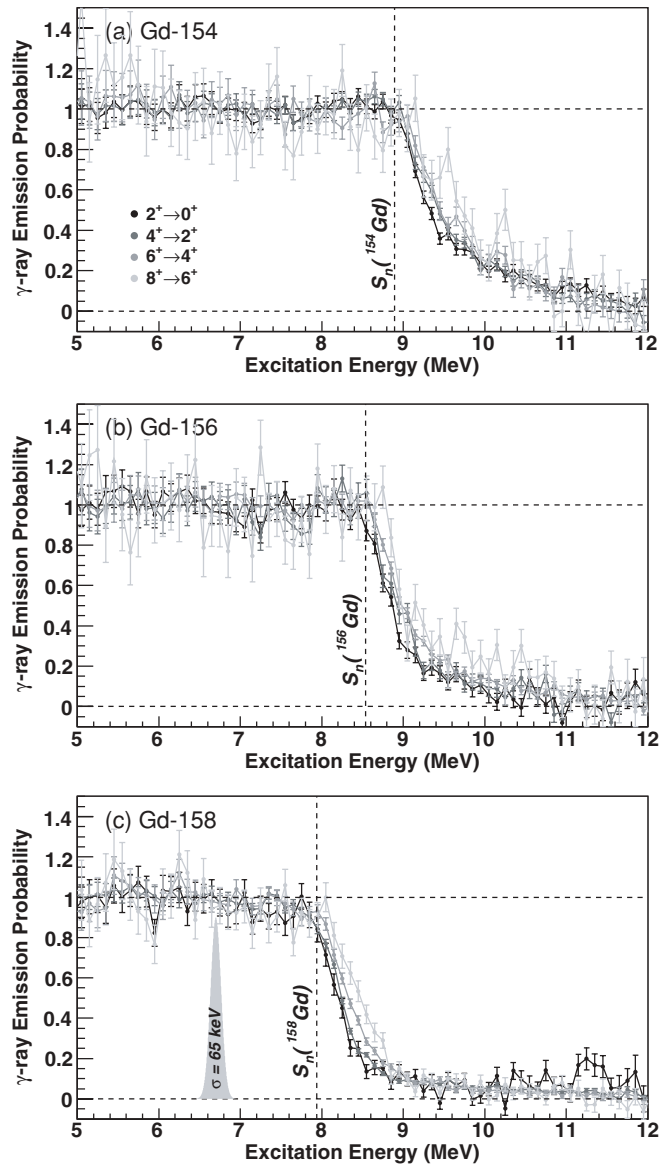


FIG. 7.  $\gamma$ -ray emission probability from compound nuclei (a)  $^{154}\text{Gd}$ , (b)  $^{156}\text{Gd}$ , and (c)  $^{158}\text{Gd}$  from 5–12 MeV as determined from the lowest four ground-state band transitions. For each isotope and each transition, the probability was normalized to unity for energies below  $S_n$  by appropriate values for  $f(E_{\text{ex}})$  [see Eq. (6)]. For comparison, the resolution ( $\sigma = 65$  keV) with which the excitation energy was determined is also shown.

is dominated by statistics. The largest systematic uncertainties were from  $f(2\text{--}4\% \times E_n [\text{MeV}])$  and background subtractions ( $<10\%$ ). Note that  $\epsilon_\gamma$  and its associated uncertainty merely affects the scaling for  $f$  required to cause  $P_{\delta\gamma} = 1$  below  $S_n$  and does not affect  $P_{\delta\gamma}$  itself.

### B. Weisskopf-Ewing approximation

The validity and limitations of the WE approximation were investigated by substituting the measured  $P_{\delta\gamma}$  values for the branching ratio  $G_\gamma^{\text{CN}}$  and multiplying by a calculated  $\sigma_n^{\text{CN}}$  as prescribed by Eq. (4). In Fig. 8, the resulting  $^{155,157}\text{Gd}(n,\gamma)$

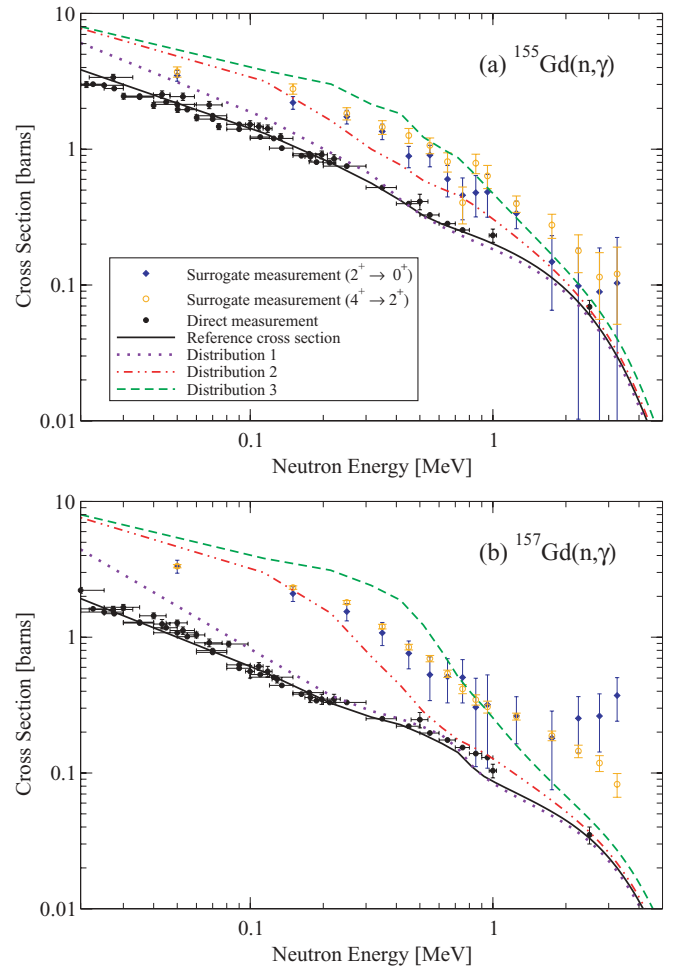


FIG. 8. (Color online) Cross sections for (a)  $^{155}\text{Gd}(n,\gamma)$  and (b)  $^{157}\text{Gd}(n,\gamma)$  reactions. The cross sections obtained from a WE analysis of the surrogate data (blue diamonds) are compared to direct measurements (black circles) and Hauser-Feshbach calculations (black solid lines). Cross sections obtained from a WE analysis of simulated surrogate measurements with three sample spin-parity distributions ( $p = 1, 2, 3$  explained later in the text) are shown as well.

cross sections are compared to directly measured results, which extend up to 2.5 MeV [21,22]. For neutron energies below about 1.5 MeV, the extracted cross sections are consistently too large, on average, by factors of roughly 2.0 and 3.4 for  $^{155}\text{Gd}$  and  $^{157}\text{Gd}$ , respectively. At higher energies where the WE conditions are closer to being satisfied, the statistics become too poor to make definite statements about the agreement for  $^{155}\text{Gd}$  and seem to remain too large for  $^{157}\text{Gd}$ .

Hauser-Feshbach-type calculations were carried out to provide insight into the origin of the discrepancies between the directly measured cross sections and those extracted from a WE analysis of the surrogate data. Standard calculations for the  $^{155,157}\text{Gd}(n,\gamma)$  cross sections were performed using relevant structure information (such as the energies of discrete levels,  $\gamma$  branching ratios, resonance information, etc.) obtained from the Reference Input Parameter Library (RIPL)-3 database [36].

Level density and strength function parameters were adjusted to reproduce the known  $s$ -wave resonance spacings, average radiative widths, and measured cross sections. The resulting  $(n, \gamma)$  cross sections (shown as black lines in Fig. 8) are in excellent agreement with the direct measurements (black filled circles) for both isotopes.

Since the Hauser-Feshbach description of the decay of a compound nucleus by  $\gamma$ -ray emission and neutron evaporation (proton or  $\alpha$ -particle emission is negligible at these energies) keeps track of angular momentum and parity of the system, it is possible to extract  $G_\gamma^{\text{CN}}(E_{\text{ex}}, J, \pi)$  from the calculation for each relevant  $J^\pi$  combination, as a function of energy. Only the calculated  $G_\gamma^{\text{CN}}(E_{\text{ex}}, J, \pi)$  values for  $J^\pi = 0^+, 2^+, 4^+, 6^+, 8^+$  and  $J^\pi = 1^-, 3^-, 5^-, 7^-, 9^-$  are shown in Fig. 9 because the inelastic scattering mechanism employed in the surrogate reaction populates primarily natural-parity states. All decay probabilities are seen to drop from unity below  $S_n$  to values around  $10^{-2}$  at 2.5 MeV above  $S_n$ . The curves corresponding to small angular momenta ( $J \leq 3$ ) in the compound nucleus exhibit a steep drop-off within 100 keV of  $S_n$ . For larger values of  $J$ , the steep drop occurs at successively higher energies. For

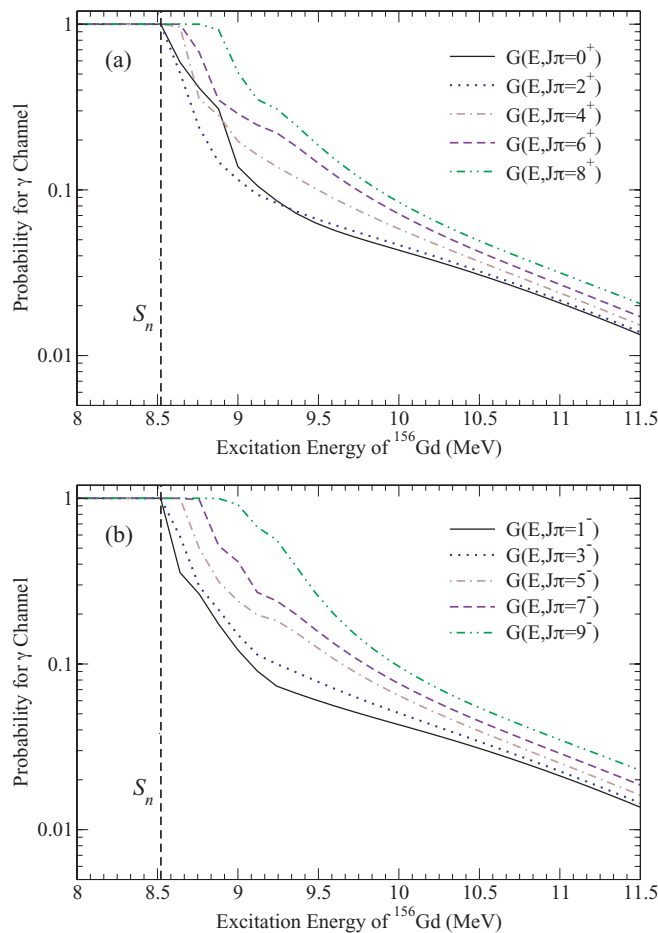


FIG. 9. (Color online) Calculated  $\gamma$ -ray emission probabilities  $G_\gamma^{\text{CN}}(E_n, J, \pi)$ , for  $^{156}\text{Gd}$ . Shown is the probability that the compound nucleus, when produced with a specific  $J^\pi$  combination, decays via the  $\gamma$  channel. Positive-parity and negative-parity probabilities are shown in (a) and (b), respectively.

energies below a few 100 keV, where  $s$ -wave neutron transmission dominates over  $p$ -wave and  $d$ -wave transmissions, neutron evaporation from those higher angular-momentum values is hindered because the residual  $^{155}\text{Gd}$  nucleus has few high- $J$  states to which the decay can occur. As the excitation energy of the compound nucleus increases,  $p$ -wave and  $d$ -wave transitions begin to compete and additional high- $J$  states become available in the neighboring nucleus, leading to a rapid decline of the  $\gamma$ -ray emission probability. The effect of individual  $^{155}\text{Gd}$  levels is also seen to disappear with increasing excitation energy. The decay probabilities for  $^{158}\text{Gd}$  display similar behavior, with a more rapid drop than observed for  $^{156}\text{Gd}$ , and somewhat larger differences between the curves corresponding to different angular-momentum values.

The measured ground-state band  $\gamma$ -ray transitions display similar energy shifts with increasing angular momentum of the initial state (see Fig. 7). This indicates that the different transitions “sample” different compound-nucleus  $J^\pi$  distributions. This is expected because states with higher spins are primarily populated in compound nuclei created with higher angular momenta as a result of the selection rules of the  $E1$  transitions that dominate the cascade. Of course, the higher- $J$  transitions, such as  $8^+ \rightarrow 6^+$ , subsequently lead to lower- $J$  transitions as all cascades ultimately reach the  $0^+$  ground state. In particular, the  $2^+ \rightarrow 0^+$  transition is a part of most cascades and therefore contains contributions from essentially all compound-nuclear  $J^\pi$  states. In fact, the  $\gamma$ -ray distributions provide a signature of the  $J^\pi$  distribution of the compound nucleus formed in the surrogate reaction.

If the surrogate reaction imparts more angular momentum to the compound nucleus than the corresponding neutron-induced reaction, the  $J \rightarrow J-2$  ground-state band transitions at the bottom of the  $\gamma$ -ray cascade will (in general) be fed by higher angular momentum states. The measured decay probabilities  $P_{\delta\gamma}(E_{\text{ex}})$  of Eq. (3) will therefore contain correspondingly larger contributions from those  $G_\gamma^{\text{CN}}(E_{\text{ex}}, J, \pi)$  associated with these larger  $J$  values. Because the desired low-energy neutron-induced reaction involves low spins (see Fig. 10), the cross section extracted by approximating  $P_{\delta\gamma}(E_{\text{ex}}) \approx G_\gamma^{\text{CN}}(E_{\text{ex}})$  will typically give too large a result. The  $2^+ \rightarrow 0^+$  transition samples a  $J^\pi$  distribution that is closest to the desired one but still yields cross sections that are too large by factors of 2 to 4 as discussed earlier (see Fig. 8). Extracting a cross section from the measured  $4^+ \rightarrow 2^+$  or  $6^+ \rightarrow 4^+$  transition strengths will lead to even more significant deviations from the directly measured cross section as is apparent from the larger exit-channel branching ratios.

The effect of the  $J^\pi$  mismatch between the desired and surrogate reactions on the cross section extracted from a WE analysis was simulated by employing the calculated  $G_\gamma^{\text{CN}}(E_{\text{ex}}, J, \pi)$  of Fig. 9 and the three schematic, energy-independent surrogate spin-parity distributions  $F_\delta^{\text{CN(p)}}(E_{\text{ex}}, J, \pi)$ , shown in Fig. 10, to determine the simulated surrogate coincidence probabilities,  $P_{\delta\gamma}^{(p)}(E_{\text{ex}})$ , from Eq. (3). The  $F_\delta^{\text{CN(p)}}(E_{\text{ex}}, J, \pi)$  distributions chosen for this sensitivity study consist only of the natural-parity states expected from the inelastic scattering reaction and have widths similar to the neutron-induced reaction, but have different

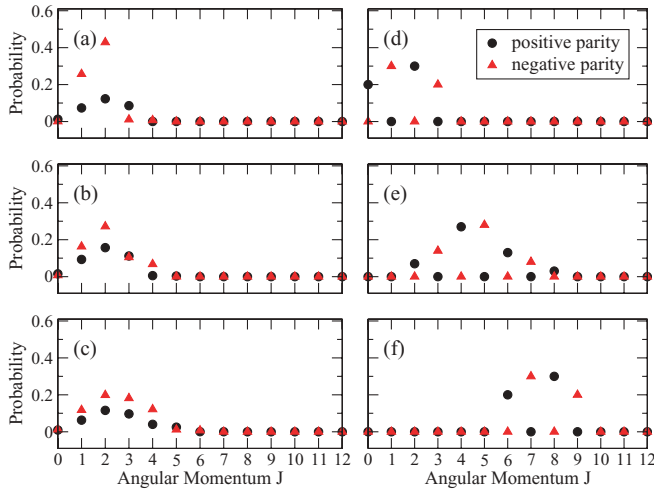


FIG. 10. (Color online) Spin-parity distributions of the compound nucleus  $^{156}\text{Gd}$ . Calculated distributions for the desired, neutron-induced, reaction are shown for neutron energies (a)  $E_n = 0.1$ , (b) 0.5, and (c) 1.5 MeV. Schematic spin-parity distributions (d)  $p = 1$ , (e)  $p = 2$ , and (f)  $p = 3$ , consisting of natural-parity states were selected to simulate possible surrogate-reaction distributions.

average values of  $J$  to simulate possible surrogate-reaction distributions. Using this  $P_{\delta\gamma}^{(p)}$  result in Eq. (4), the  $^{155}\text{Gd}(n,\gamma)$  cross sections indicated in Fig. 8(a) by the dotted ( $p = 1$ ), dash-dotted ( $p = 2$ ), and dashed ( $p = 3$ ) curves, respectively, are obtained. The results for the  $^{157}\text{Gd}(n,\gamma)$  cross section are shown in Fig. 8(b). At energies below about 1.5 MeV, the calculated cross sections vary by up to a factor of 4 for  $^{155}\text{Gd}$  and up to a factor of 6 for  $^{157}\text{Gd}$ . This variation gives a rough estimate of the uncertainty that can result when extracting an  $(n,\gamma)$  cross section from a WE analysis of surrogate data, for nuclei of the type (nonfissioning, deformed) considered here. Of course, the actual deviation from the true cross section depends on the  $J^\pi$  mismatch between the reactions; the deviations can be much smaller if the  $J^\pi$  differences are minimized. The  $p = 1$  distribution that resembles the neutron-induced situation the most produces the best agreement with the data. Clearly, it is preferable to carry out an experiment with a reaction mechanism and experimental conditions (projectile energy, angle of outgoing direct-reaction particle) that create  $J^\pi$  distributions similar to the one produced in the desired reaction. The cross sections extracted from this measurement (blue circles) fall, for the most part, between the calculated curves. They are somewhat larger than the curve for distribution  $p = 2$ , but smaller than the curve for  $p = 3$ , a result that is consistent with the previous discussion. The cross sections obtained from the simulations  $p = 1, 2, 3$  are seen to converge for energies larger than about 1.5 MeV (i.e., the dependence on the spin-parity distribution decreases and the WE assumption becomes a better approximation). The experimental results seem high in this energy region, but the statistical uncertainty from the measurement becomes too large to draw more detailed conclusions.

The factor by which the WE approach overestimates the cross section is quite different for the two cases considered

here, even though the same reaction mechanism and experimental setup was used and the two nuclei have very similar structure properties. Unfortunately, this makes it, at present, impossible to determine a simple predictive procedure (such as straightforward scaling) for correcting the  $(n,\gamma)$  cross sections extracted in a WE analysis. It also casts doubt on the success of any method that relies on comparing similar reactions on similar nuclei to obtain  $(n,\gamma)$  cross sections.

These arguments also indicate that the  $^{233}\text{Pa}(n,\gamma)$  cross section in Ref. [19], which was obtained from a WE analysis of a  $^{232}\text{Th}(^3\text{He},p)^{234}\text{Pa}$  surrogate experiment is likely to be overestimated, perhaps by as much as a factor of 2. A smaller cross section will be more in line with the statistical-model calculations [19].

### C. Surrogate ratio approximation

In the *surrogate ratio approach* [3,8], two surrogate experiments are performed to determine the ratio of two cross sections of compound-nuclear reactions. An independent determination of one cross section can then be used to deduce the other from the ratio. The ratio method can also be used to circumvent the need to measure  $N_\delta$ , which can be difficult due to backgrounds caused by target backings or impurities. An underlying assumption was that this method reduces the effects of the  $J^\pi$  mismatch to a level where it can be neglected. For  $(n, f)$  cross sections, there are indications that small to moderate deviations from the WE assumption might cancel [3], and in fact, the results are consistent with direct measurements [11] as well as complementary surrogate experiments [8].

In the WE limit, the ratio  $R(E)$  of the  $(n,\gamma)$  cross sections is

$$R(E) = \frac{\sigma_n^{\text{CN1}}(E)G_\gamma^{\text{CN1}}(E)}{\sigma_n^{\text{CN2}}(E)G_\gamma^{\text{CN2}}(E)}, \quad (9)$$

with branching ratios  $G_\gamma^{\text{CN}}(E)$  that are independent of  $J$  and  $\pi$  and compound-nucleus formation cross sections  $\sigma_\gamma^{\text{CN1}}$  and  $\sigma_\gamma^{\text{CN2}}$  that can be calculated by using an optical model. Often, it is assumed that  $\sigma_n^{\text{CN1}}/\sigma_n^{\text{CN2}} \approx 1$ , and therefore the ratio is determined solely from the ratio of exit-channel probabilities.

Here, the ratio method is tested by comparing the ratio of the measured exit-channel probabilities to the ratio  $R^{\text{ref}} = \sigma_{n\gamma}^{158\text{Gd}}(E)/\sigma_{n\gamma}^{156\text{Gd}}(E)$  of the reference cross sections (black solid lines in Fig. 8). The comparison is shown in Fig. 11. The impact of a  $J^\pi$  mismatch is explored and compared to complementary calculations for the first time.

For neutron energies below about 1 MeV, the experimentally determined ratio is approximately unity, which is as much as a factor of 2 larger than the reference ratio. Therefore, if one extracted the low-energy  $^{157}\text{Gd}(n,\gamma)$  cross section from this ratio, the result will be too large by this same factor. To better assess the uncertainty that results from neglecting the  $J^\pi$  mismatch between desired and surrogate reactions, the ratios of the simulated WE cross sections,  $R^p = \sigma_{n\gamma}^{158\text{Gd}(p)} / \sigma_{n\gamma}^{156\text{Gd}(p)}$  for the three schematic spin-parity distributions  $p = 1, 2, 3$  shown in Fig. 10 were calculated. The ratios, plotted in Fig. 11, are seen to differ from each other by up to a factor of

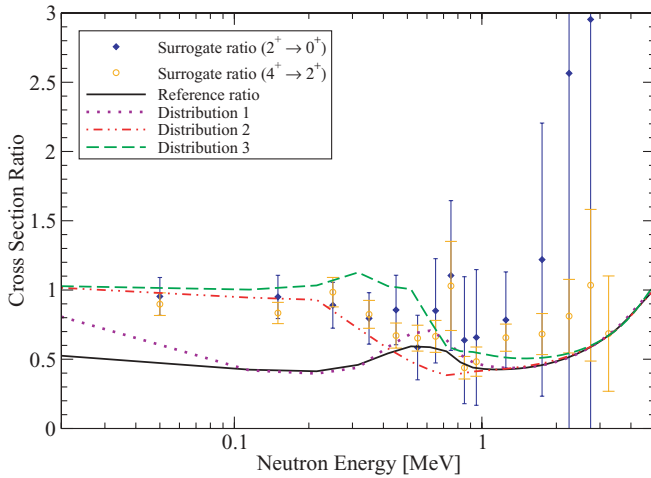


FIG. 11. (Color online) Ratio of  $^{157}\text{Gd}(n,\gamma)$  and  $^{155}\text{Gd}(n,\gamma)$  cross sections. The ratio obtained from the present data (blue diamonds) is compared to the ratio  $R^{\text{ref}}$  (black solid line) of the reference cross sections from Fig. 8. Also shown are the ratios  $R^p$  of the simulated coincidence probabilities, for the distributions  $p = 1, 2, 3$  given in Fig. 10.

2.5 for energies below about  $E_n = 0.7$  MeV; above that energy, they rapidly converge to the expected result. Thus, the ratio approach seems to somewhat reduce the effect of the  $J^\pi$  mismatch on the extracted cross sections for energies where the WE approximation is not valid.

An additional issue of concern arises that was overlooked in some surrogate ratio analyses because the ratio  $R(E)$  can be defined either at *the same equivalent neutron energy*  $E_n$  in the numerator and denominator, or *the same excitation energy*  $E_{\text{ex}}$ . Of course, the two energies are simply related by Eq. (2). However, when cross sections for two nuclei with *different* separation energies  $S_{n_1}$  and  $S_{n_2}$  are compared, the energy choice can introduce additional uncertainty in either the ratio of formation cross sections or the ratio of exit-channel branching ratios. For  $(n,\gamma)$  cross sections, which vary rapidly in energy,  $E_n$  is the natural choice and  $\sigma_n^{\text{CN1}}/\sigma_n^{\text{CN2}} \approx 1$  at all energies (for neutron-induced reactions on similar targets). However, the ratio  $G_\gamma^{\text{CN1}}/G_\gamma^{\text{CN2}}$  is obtained from an experiment that measures quantities in terms of  $E_{\text{ex}}$ , a fact that complicates the analysis if  $E_n$  is selected to define  $R(E)$ . In previous experiments [17,18], the ratio  $G_\gamma^{\text{CN1}}/G_\gamma^{\text{CN2}}$  was inferred from the ratio of coincidence counts  $N_{\delta\gamma}$  and not the individual decay probabilities  $G_\gamma^{\text{CN1}}$  and  $G_\gamma^{\text{CN2}}$  because the particle-singles counts  $N_\delta$  cannot be reliably determined. Therefore, comparing  $N_{\delta\gamma}$  at  $E_n$  meant comparing the two reactions at outgoing particles energies that differ by  $\Delta E = S_{n_1} - S_{n_2}$ , which was hundreds of keV in Refs. [17,18], but can be several MeV in more extreme cases. The particle detection efficiency and  $N_\delta$  may vary in ways that were not measured and may be difficult to estimate. Note that defining  $R(E)$  instead in terms of  $E_{\text{ex}}$  introduces different issues. In particular, the energy dependence of the ratio of the formation cross sections,  $\sigma_n^{\text{CN1}}/\sigma_n^{\text{CN2}}$ , which appears in Eq. (9), has to be taken into account explicitly.

In the experiment presented here, the ratio  $R(E)$  was determined at the same equivalent neutron energy for  $^{155}\text{Gd}(n,\gamma)$  and  $^{157}\text{Gd}(n,\gamma)$ . The choice of energy at which experimental results are compared does not introduce the uncertainties discussed previously because  $G_\gamma^{\text{CN1}}$  and  $G_\gamma^{\text{CN2}}$  were independently obtained directly from  $N_{\delta\gamma}$  and  $N_\delta$ . The  $^{155}\text{Gd}$  and  $^{157}\text{Gd}$  nuclei are structurally very similar, they are well-deformed and both have ground-state spin and parity  $J^\pi = 3/2^-$ , so  $\sigma_n^{155\text{Gd}}/\sigma_n^{157\text{Gd}} \approx 1$  was expected to be a good approximation.

Results of the ratio method were recently compared to directly measured  $(n,\gamma)$  cross sections for dysprosium and ytterbium isotopes. In Refs. [18] and [37], the feasibility of using  $(d, p\gamma)$  as a surrogate reaction to determine  $(n,\gamma)$  cross sections was explored. Results for the  $^{171}\text{Yb}(n,\gamma)/^{173}\text{Yb}(n,\gamma)$  cross-section ratio were compared to the directly measured cross-section ratio at energies up to 300 keV. Because the  $2^+ \rightarrow 0^+$  transition in the  $^{172,174}\text{Yb}$  compound nuclei was highly converted ( $\alpha_{\text{IC}} > 8$ ), only transitions from higher- $J$  states ( $4^+ \rightarrow 2^+$  and  $6^+ \rightarrow 4^+$ ) had sufficient statistics for the analysis. The results display trends similar to those calculated and shown in Fig. 11—the ratios are consistent with unity and the  $6^+ \rightarrow 4^+$  transition yielded a higher cross section. It was noted that subtracting the feeding from the  $6^+$  state to the  $4^+$  state will likely select a compound-nuclear  $J^\pi$  distribution closer to the one populated by the neutron-induced reaction. Indeed, the cross-section result was in closer agreement to the directly measured results when the  $4^+ \rightarrow 2^+$  transition was used with the  $6^+ \rightarrow 4^+$  transition intensity subtracted [37]. In Ref. [17],  $^{161}\text{Dy}$  and  $^{171}\text{Yb}$  compound nuclei were populated using  $(^3\text{He}, ^3\text{He}')$  and  $(^3\text{He}, \alpha)$  reactions. In this experiment, statistical  $\gamma$  rays with energy  $> 1.5$  MeV were used to identify the exit channel. The  $^{170}\text{Yb}(n,\gamma)$  cross section, determined relative to the  $^{160}\text{Dy}(n,\gamma)$  cross section was consistent with directly measured results for both surrogate reactions. Again, like the results of the statistical-model calculation presented here, the inferred cross-section ratios were consistent with unity (within the 30–50% experimental uncertainties) below 0.5 MeV.

#### D. $^{153}\text{Gd}$ cross section

Given the large discrepancies between the  $^{155,157}\text{Gd}(n,\gamma)$  cross sections obtained from either a WE or ratio analysis of the data and the directly measured results, only a crude measure of the  $^{153}\text{Gd}(n,\gamma)$  cross section can be determined by applying these approximate methods to the available  $^{154}\text{Gd}(p, p\gamma)$  data. Based solely on the  $P_{\delta\gamma}$  values, this cross section is expected to be roughly 1.5 times larger than the  $^{155}\text{Gd}(n,\gamma)$  cross section. This is consistent with the ratio of  $1.72 \pm 0.26$  for these Maxwellian-averaged  $(n,\gamma)$  cross sections at 30-keV thermal energies listed in the compilation of Ref. [38] and based on a calculation of the  $^{153}\text{Gd}(n,\gamma)$  cross section. This larger value makes sense intuitively because  $S_n$  for  $^{154}\text{Gd}$  is 500 keV higher than for  $^{156}\text{Gd}$ , which leads to an increased level density and favors  $\gamma$ -ray emission. However, without a more sophisticated surrogate analysis that accounts for  $J^\pi$  effects, a reliable  $(n,\gamma)$  cross-section result cannot be quoted.

## V. CONCLUSION

Surrogate ( $p, p'$ ) measurements were carried out for several gadolinium isotopes, which allowed tests of approximations that were recently employed in the interpretation of surrogate data. While the WE and surrogate ratio approximations were successfully used to determine ( $n, f$ ) cross sections for a variety of actinide nuclei, the low-energy ( $n, \gamma$ ) cross sections obtained here for nonfissioning well-deformed nuclei are not in good agreement with results from direct measurements. In particular, results obtained using the WE approximation are consistently too high, a discrepancy that can be understood with the help of the Hauser-Feshbach-type calculations presented here. Even for the  $^{155}\text{Gd}$  and  $^{157}\text{Gd}$  measurements that were performed using the same experimental setup on nuclei with very similar nuclear structure properties, the factor by which the WE approach overestimates the cross section was different. For energies above 1.5 MeV, the calculations indicate that the WE approximation may be valid, but the statistical uncertainties of the data do not allow a definitive conclusion. Further experiments with better statistics for this energy regime will help to elucidate the issue.

The ratio approach, which was successfully employed for obtaining ( $n, f$ ) cross sections, is seen to reduce the discrepancy between the extracted and reference ( $n, \gamma$ ) cross sections. The data and calculations presented here show that the effects of the  $J^\pi$  mismatch between desired and surrogate reactions can still be significant for energies below about 0.7 MeV; discrepancies on the order of a factor of 2 were observed. However, the calculations indicate that the WE assumption, coupled with a ratio analysis will approach the desired cross section at lower energies than a WE analysis

alone. This might prove useful for obtaining some data points that make it possible to constrain calculation of an unknown ( $n, \gamma$ ) cross section.

These results demonstrate that, in general, the effects caused by the  $J^\pi$  differences between the neutron-induced and surrogate reactions cannot be neglected. Techniques that address angular-momentum effects are currently being developed to move beyond the limitations uncovered here. In addition, experiments should be designed to minimize contributions from spins that are not relevant to low-energy ( $n, \gamma$ ) reactions, such as by focusing on observing  $\gamma$  rays from transitions between the low angular-momentum members of the ground-state band. Due to the limitations of the WE and ratio approximations, no  $^{153}\text{Gd}(n, \gamma)$  cross section is quoted here. It is only noted that the  $\gamma$ -ray exit-channel branching ratio is larger for  $^{154}\text{Gd}$  than for  $^{156}\text{Gd}$ , which is consistent with published estimates.

## ACKNOWLEDGMENTS

We thank the 88-Inch Cyclotron operations and staff at Lawrence Berkeley National Laboratory for their support in performing these experiments. A.O. Macchiavelli's contributions to the development of STARS/LiBerACE are gratefully acknowledged. This work was performed under the auspices of the US Department of Energy by Lawrence Livermore National Laboratory in part under Contract No. W-7405-Eng-48 and in part under Contract No. DE-AC52-07NA27344 and the University of California DOE Contract No. DE-AC0376SF0098 and the University of Richmond Contract Nos. DE-FG-05NA25929 and DE-FG02-05ER41379.

- 
- [1] E. M. Burbidge, G. R. Burbidge, W. A. Fowler, and F. Hoyle, *Rev. Mod. Phys.* **29**, 547 (1957).
  - [2] G. Wallerstein *et al.*, *Rev. Mod. Phys.* **69**, 995 (1997).
  - [3] J. E. Escher and F. S. Dietrich, *Phys. Rev. C* **74**, 054601 (2006).
  - [4] J. Escher, *AIP Conf. Proc.* **1005**, 83 (2008).
  - [5] J. D. Cramer and H. C. Britt, *Nucl. Sci. Eng.* **41**, 177 (1970).
  - [6] H. C. Britt and J. B. Wilhelmy, *Nucl. Sci. Eng.* **72**, 222 (1979).
  - [7] M. Petit *et al.*, *Nucl. Phys. A* **735**, 345 (2004).
  - [8] J. T. Burke *et al.*, *Phys. Rev. C* **73**, 054604 (2006).
  - [9] B. Jurado *et al.*, *AIP Conf. Proc.* **1005**, 90 (2008).
  - [10] M. S. Basunia *et al.*, *Nucl. Instrum. Methods Phys. Res., Sect. B* **267**, 1899 (2009).
  - [11] S. R. Lesher *et al.*, *Phys. Rev. C* **79**, 044609 (2009).
  - [12] B. L. Goldblum *et al.*, *Phys. Rev. C* **80**, 044610 (2009).
  - [13] W. Younes and H. C. Britt, *Phys. Rev. C* **67**, 024610 (2003).
  - [14] W. Younes and H. C. Britt, *Phys. Rev. C* **68**, 034610 (2003).
  - [15] C. Forssen, F. S. Dietrich, J. Escher, R. D. Hoffman, and K. Kelley, *Phys. Rev. C* **75**, 055807 (2007).
  - [16] J. E. Escher and F. S. Dietrich, *Phys. Rev. C* **81**, 024612 (2010).
  - [17] B. L. Goldblum, S. G. Prussin, U. Agvaanluvsan, L. A. Bernstein, D. L. Bleuel, W. Younes, and M. Guttormsen, *Phys. Rev. C* **78**, 064606 (2008).
  - [18] R. Hatarik *et al.*, *AIP Conf. Proc.* **1005**, 105 (2008).
  - [19] S. Boyer *et al.*, *Nucl. Phys. A* **775**, 175 (2006).
  - [20] J. M. Allmond *et al.*, *Phys. Rev. C* **79**, 054610 (2009).
  - [21] H. Beer and R. L. Macklin, *Astrophys. J.* **331**, 1047 (1988).
  - [22] J. Voignier, S. Joly, and G. Grenier, *Nucl. Sci. Eng.* **112**, 87 (1992).
  - [23] W. Hauser and H. Feshbach, *Phys. Rev.* **87**, 366 (1952).
  - [24] V. F. Weisskopf and P. H. Ewing, *Phys. Rev.* **57**, 472 (1940).
  - [25] S. R. Lesher *et al.* *Nucl. Instrum. Methods A* (accepted for publication).
  - [26] N. D. Scielzo *et al.*, *AIP Conf. Proc.* **1005**, 109 (2008).
  - [27] G. Duchene *et al.*, *Nucl. Instrum. Methods A* **432**, 90 (1999).
  - [28] Z. Elekes *et al.*, *Nucl. Instrum. Methods Phys. Res., Sect. A* **503**, 580 (2003).
  - [29] <http://www.ornl.gov/sci/isotopes>.
  - [30] <http://www.micronsemiconductor.co.uk>.
  - [31] National Nuclear Data Center, Brookhaven National Laboratory, [www.nndc.bnl.gov](http://www.nndc.bnl.gov).
  - [32] C. Lee and N. R. Fletcher, *Nucl. Instrum. Methods Phys. Res. A* **432**, 313 (1999).
  - [33] F. S. Goulding, D. A. Landis, J. Cerny, and R. H. Pehl, *Nucl. Instrum. Methods* **31**, 1 (1964).
  - [34] 88-Inch Cyclotron operators (private communication).
  - [35] T. Kibedi, T. W. Burrows, M. B. Trzhaskovskaya, P. M. Davidson, and C. W. Nestor, *Nucl. Instrum. Methods Phys. Res. A* **589**, 202 (2008).
  - [36] R. Capote *et al.*, *Nucl. Data Sheets* **110**, 3107 (2009).
  - [37] R. Hatarik *et al.*, *Phys. Rev. C* **81**, 011602(R) (2010).
  - [38] Z. Y. Bao *et al.*, *At. Data Nucl. Data Tables* **76**, 70 (2000).